

# Northumbria Research Link

Citation: Hou, Chuanxin, Yang, Wenyue, Kimura, Hideo, Xie, Xiubo, Zhang, Xiaoyu, Sun, Xueqin, Yu, Zhipeng, Yang, Xiaoyang, Zhang, Yuping, Wang, Bin, Xu, Bin, Sridhar, Deepak, Algadi, Hassan, Guo, Zhanhu and Du, Wei (2023) Boosted lithium storage performance by local build-in electric field derived by oxygen vacancies in 3D holey N-doped carbon structure decorated with molybdenum dioxide. *Journal of Materials Science and Technology*, 142. pp. 185-195. ISSN 1005-0302

Published by: Elsevier

URL: <https://doi.org/10.1016/j.jmst.2022.10.007>  
<<https://doi.org/10.1016/j.jmst.2022.10.007>>

This version was downloaded from Northumbria Research Link:  
<https://nrl.northumbria.ac.uk/id/eprint/50464/>

Northumbria University has developed Northumbria Research Link (NRL) to enable users to access the University's research output. Copyright © and moral rights for items on NRL are retained by the individual author(s) and/or other copyright owners. Single copies of full items can be reproduced, displayed or performed, and given to third parties in any format or medium for personal research or study, educational, or not-for-profit purposes without prior permission or charge, provided the authors, title and full bibliographic details are given, as well as a hyperlink and/or URL to the original metadata page. The content must not be changed in any way. Full items must not be sold commercially in any format or medium without formal permission of the copyright holder. The full policy is available online: <http://nrl.northumbria.ac.uk/policies.html>

This document may differ from the final, published version of the research and has been made available online in accordance with publisher policies. To read and/or cite from the published version of the research, please visit the publisher's website (a subscription may be required.)

# **Boosted lithium storage performance by local build-in electric field derived by oxygen vacancies in 3D holey N-doped carbon structure decorated with molybdenum dioxide**

Chuanxin Hou<sup>a#\*</sup>, Wenyue Yang<sup>a#</sup>, Hideo Kimura<sup>a</sup>, Xiubo Xie<sup>a</sup>, Xiaoyu Zhang<sup>a,b</sup>, Xueqin Sun<sup>a</sup>, Zhipeng Yu<sup>a</sup>, Xiaoyang Yang<sup>a</sup>, Yuping Zhang<sup>a</sup>, Bin Wang<sup>c, d</sup>, Ben Bin Xu<sup>e</sup>, Deepak Sridhar<sup>f</sup>, Hassan Algadi<sup>g</sup>, Zhanhu Guo<sup>c, e\*</sup> and Wei Du<sup>a\*</sup>

- a. School of Environmental and Material Engineering, Yantai University, No. 30 Qingquan Road, Yantai, Shandong, 264005, China
- b. Shandong Laboratory of Yantai Advanced Materials and Green Manufacturing, Yantai, Shandong, 264005, China
- c. Integrated Composites Laboratory (ICL), Department of Chemical & Biomolecular Engineering, University of Tennessee, Knoxville, TN 37996, USA
- d. College of Materials Science and Engineering, Taiyuan University of Science and Technology, Taiyuan, 030024, Shanxi, China
- e. Mechanical and Construction Engineering, Faculty of Engineering and Environment, Northumbria University, Newcastle Upon Tyne, NE1 8ST, UK
- f. Zentek Ltd. 24 Corporate Court, Guelph, Ontario, N1G 5G5 Canada
- g. Department of Electrical Engineering, Faculty of Engineering, Najran University, Najran, 11001, Saudi Arabia

# These authors contributed equally.

## **Corresponding Authors:**

Chuanxin Hou: [chuanxin210@ytu.edu.cn](mailto:chuanxin210@ytu.edu.cn) ; Zhanhu Guo: [nanomaterials2000@gmail.com](mailto:nanomaterials2000@gmail.com) ; Wei Du: [duwei@ytu.edu.cn](mailto:duwei@ytu.edu.cn)

## Abstract

Three-dimensional holey nitrogen-doped carbon matrix decorated with molybdenum dioxide ( $\text{MoO}_2$ ) nanoparticles have been successfully synthesized via a NaCl-assisted template strategy. The obtained  $\text{MoO}_2/\text{C}$  composites offered multi-advantages, including higher specific surface area, more active sites, more ions/electrons transmission channels, and shorter transmission path due to the synergistic effect of the uniformly distributed  $\text{MoO}_2$  nanoparticles and porous carbon structure. Especially, the oxygen vacancies were introduced into the prepared composites, and enhanced the  $\text{Li}^+$  intercalation/deintercalation process during electrochemical cycling by Coulomb force. The existence of local build-in electric field was proved by experimental data, differential charge density distribution and density of states calculation. The unique designed structure and introduced oxygen vacancy defects endowed the  $\text{MoO}_2/\text{C}$  composites with excellent electrochemical properties. In view of the synergistic effect of the unique designed morphology and introduced oxygen vacancy defects, the  $\text{MoO}_2/\text{C}$  composites exhibited superior electrochemical performance of a high capacity of  $918.2 \text{ mAh g}^{-1}$  at  $0.1 \text{ A g}^{-1}$  after 130 cycles,  $562.1 \text{ mAh g}^{-1}$  at  $1.0 \text{ A g}^{-1}$  after 1000 cycles and a capacity of  $181.25 \text{ mAh g}^{-1}$  even at  $20.0 \text{ A g}^{-1}$ . This strategy highlights the path to promote the commercial application of  $\text{MoO}_2$ -based and other transition metal oxides electrodes for energy storage devices.

**Keywords** :  $\text{MoO}_2/\text{C}$  Hybrid; 3D Holey Structure; Oxygen Vacancies; Lithium-ion Batteries.

## 1. Introduction

Faced with enormous challenges of the ever-increasing energy shortage crisis and increasing environmental problems, immense efforts have been made to seek and enhance the reliability and practicability of new generation clean energy [1-5]. Meanwhile, the energy storages are sought-after to fill the timeliness of new energy, including wind, solar, nuclear, geothermal, etc [6, 7]. Among multitudinous optional candidates, lithium-ion batteries (LIBs) have been proved to a great success as energy storage equipment for electronic mobile devices and electric vehicle [8-10]. To substitute commercial graphite anode with the low theoretical specific capacity ( $372 \text{ mAh g}^{-1}$ ) [11], numerous kinds of anode materials were designed and meliorated to meet the demands of higher energy density and power density LIBs [12].

Transition metal oxides (TMOs) have been investigated over the past few decades as electrodes for LIBs on account of the superiorities of high specific capacity, environmentally friendly, abundant resources, easy synthesis and cost effective [13]. Especially, the common power cut-off phenomenon in modern society is urging higher performance LIBs anodes to put into the market, which further broadens the development prospects and research significance of TMOs. Among multifarious TMOs, molybdenum dioxide ( $\text{MoO}_2$ ) has attracted more attention based on its characteristic of high theoretical specific capacity ( $838 \text{ mAh g}^{-1}$ ), satisfactory chemical stability and relatively high electronic conductivity ( $>1 \times 10^4 \text{ S cm}^{-1}$ ), which are precondition for next generation LIBs anodes [14]. Unlike commercial graphite anodes with the  $\text{Li}^+$  intercalation/deintercalation via intercalation reaction, the

reversibly inserts/extracts of  $\text{Li}^+$  in  $\text{MoO}_2$  by the conversion reaction, as shown in formula (1) and (2) [15, 16]:



which contains phase change of  $\text{MoO}_2$ , formation/decomposition of  $\text{Li}_2\text{O}$ , and redox of metal phase. Normally, the huge volumetric changes occurred during cycling processes, which may cause the fragmentation and agglomeration of  $\text{MoO}_2$  particles, resulting in the active electrodes stripped from fluid collector and irreversible electrolyte consumption for the repeated formation/decomposition of solid electrolyte interphase (SEI). Furthermore, the discharge product of  $\text{Li}_2\text{O}$  and the bulk  $\text{MoO}_2$  results in the inherent poor conductivity of  $\text{MoO}_2$  [17]. The mentioned issues give rise to short lifespan and rapid capacity fading, which bring challenges to obtain excellent electrochemical performance of  $\text{MoO}_2$  and cause barriers for their further commercial applications.

Nanocrystallization is believed as one feasible method to overcome these issues, since the nanosized  $\text{MoO}_2$  (compared to micro-meter) can effectively shorten the transport path of electrons and ions, enlarge contact area of electrolyte/electrodes and improve the number of active sites [18]. Meanwhile, building special morphology is an important way to improve various performances of materials [19-25], the composites composed of  $\text{MoO}_2$  nanostructure and various carbonaceous materials with special morphologies are considered as another effectively strategy to deal with the aforementioned issues, thanks to the carbonaceous materials can relieve volume

expansion and improve electronic conductivity of MoO<sub>2</sub>. For example, 3D MoO<sub>2</sub>/N-doped carbon composites were prepared and delivered a high reversible Li storage capacity due to the designed 3D structure [26]. Benefiting from the unique 3D MoO<sub>2</sub>/N-doped carbon matrix structure, the volumetric changes were effectively relieved and the conductivity of MoO<sub>2</sub> was increased [14]. Indeed, the electrochemical performance of MoO<sub>2</sub> electrodes has been ameliorated effectively via embedding the MoO<sub>2</sub> nanostructure into the conductive carbon matrix. Nevertheless, the Li<sub>0.8</sub>MoO<sub>2</sub> phase with a low conductivity will be formed in its initial lithiation process, and will prevent further lithiation of MoO<sub>2</sub>, which is still a challenge for its further application.

For the sake of improving the intrinsic conductivity of MoO<sub>2</sub> electrodes, defect-creating method should be a promoting and practicable route. Defect engineering (especially oxygen vacancies), which is regarded as the effectively performance-adjustment tool, has been widely applied to catalysis, microwave absorption, energy storages, and many other fields [27-30]. The oxygen vacancies engineering gives huge potentiality for narrowing the energy bandgap, controlling carrier migration, and inducing extra energy level. It is instrumental in improving the intrinsic electronic conductivity that was proved by theoretical calculation and practical experimental results [31]. Furthermore, the oxygen vacancies can affect surface thermodynamics of transition metal oxides under the case of the unchanged initial characteristics of crystal components and structures, promoting phase transition particularly at the interfaces of electrolyte and electrodes. Besides, the local build-in

electric field can be induced by the oxygen vacancy defects, which diminishes the electrostatic repulsion and stress between adjacent atoms, improves the reaction kinetics of  $e^-$  and  $Li^+$ , and thus results in excellent electrochemical performance [32].

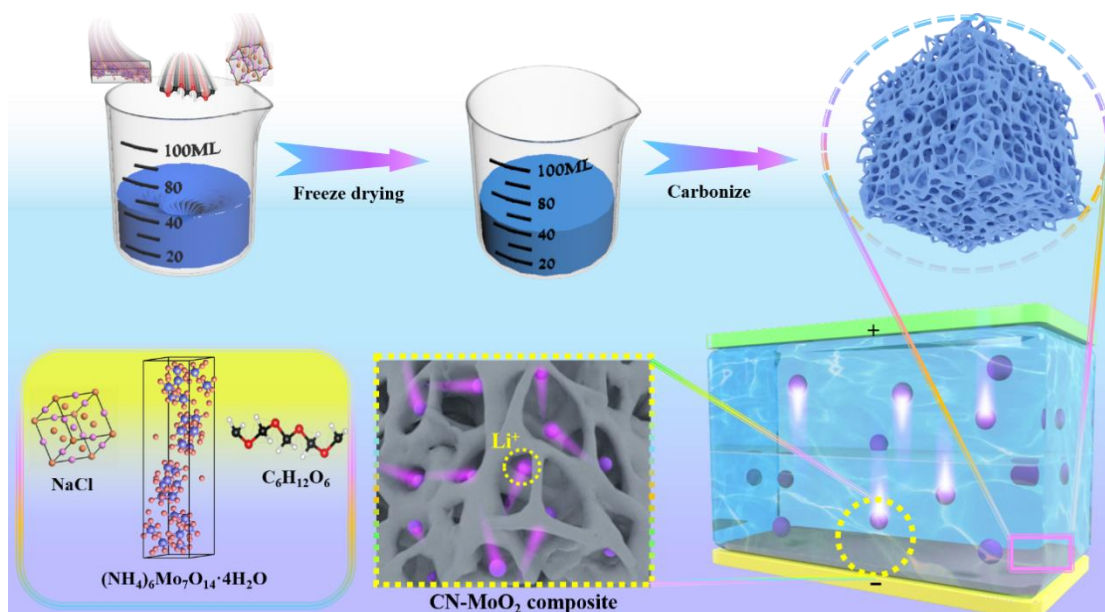
Although gigantic efforts have been devoted to upgrade the electrochemical properties of TMOs, the cooperative effects of oxygen vacancies engineering, morphology control and compound with conductive carbonaceous materials are unclear and the working mechanism of oxygen vacancies in  $MoO_2$  still need to be explored continuously and vigorously.

Herein, the oxygen vacancies-rich and three-dimensional porous nitrogen-doped carbon structure decorated with  $MoO_2$  nanoparticles (CN- $MoO_2$ ) was synthesized by the facile and controllable NaCl-assist template method. This synthetic method can yield kilogram scale product for the large amount of high-performance LIBs  $MoO_2$ -based anodes. The ingenious constructed CN- $MoO_2$  composites are predicted to provide multi-advantages for achieving satisfactory electrochemical performance when applied as anodes for LIBs. First,  $MoO_2$  nanoparticles growing inside the carbon matrix shorten the transportation path of  $Li^+$  and electrons, offer more active sites. Second, the unique designed three-dimensional porous nitrogen-doped carbon matrix can effectively reduce the influence of volumetric effect of  $MoO_2$  during cycling process, improve the electronic conductivity and the 3D honeycomb-like porous structure can also enhance the reaction kinetics by shortening the diffusion path of  $Li^+$  and electrons. Furthermore, the oxygen vacancies were introduced into the CN- $MoO_2$  composites identified by X-ray photoelectron spectroscopy and electron

paramagnetic resonance, which promoted the phase transition between MoO<sub>2</sub> and Li<sub>x</sub>MoO<sub>2</sub> in the incipient charge/discharge process and further enhanced the intrinsic conductivity of MoO<sub>2</sub>. Meanwhile, the local build-in electric field derived by oxygen vacancies proved by First principles calculation provides mass transport channels and further improves the reaction kinetics of MoO<sub>2</sub> by promoting the migration of e<sup>-</sup> and Li<sup>+</sup>. All the mentioned factors with an effective synergy will contribute to getting excellent electrochemical performance of CN-MoO<sub>2</sub> anodes and offer an effective synthetic route for MoO<sub>2</sub>-based and other TMOs electrodes for energy storage systems.

## 2. Results and Discussion

The 3D N-doped porous carbon structure attached with MoO<sub>2</sub> nanoparticles (CN-MoO<sub>2</sub> composites) was designed and successfully synthesized via a facile NaCl-assisted template method, followed with freeze-drying and carbonization processes, where the Schematic illustration is displayed in **Scheme 1**. The NaCl works as template to form the 3D porous structure and prevent agglomeration of nanoparticles. The freeze-drying process further contributes to the uniform porous structure. The carbonization process at various temperature causes the formation and disappearance of oxygen vacancies in the 3D porous matrix. The detailed preparation process has been presented in the experimental part in the supporting information.



**Scheme 1** Schematic illustration of synthetic route of CN-MoO<sub>2</sub> composites.

The morphologies of the obtained CN-MoO<sub>2</sub> composites were explored by SEM and high-resolution TEM images, as shown in **Figure 1**. All the prepared composites under different temperatures exhibited uniformly three-dimensional porous structure with smooth surface, without obvious nanoparticles as shown in Figure 1a-f (CN-MoO<sub>2</sub>-400 (a), CN-MoO<sub>2</sub>-500 (b), CN-MoO<sub>2</sub>-600 (c and d), CN-MoO<sub>2</sub>-700 (e), CN-Mo<sub>2</sub>C-800 (f)). The 3D honeycomb-like framework with an aperture of *ca.* 1  $\mu\text{m}$  of Mo-based hybrids were constructed by the interlocking network carbon nanosheets. In order to probe the detailed information of the composites, the SEM-based EDS was carried out and displayed in **Figure S1**. The observed uniform distribution of the Mo, C, N, O element indicates the formed 3D porous N-doped carbon structure and the homogeneously dispersed MoO<sub>2</sub> in 3D matrix. Figure 1g-i shows the TEM images of CN-MoO<sub>2</sub>-600 composite, further verifying morphologies and the existence of MoO<sub>2</sub> nanoparticles. The MoO<sub>2</sub> nanoparticles in the position of the yellow circle, Figure 1h, confirm the confinement growth of molybdenum dioxide particles in the carbon

matrix. The lattice fringes of 0.2171, 0.2156 and 0.2442 nm (Figure 1i), are indexed as the (021), (-212), and (200) crystal plane orientation of MoO<sub>2</sub>, respectively. All the results proved the successful construction of the 3D porous CN-MoO<sub>2</sub> composites.

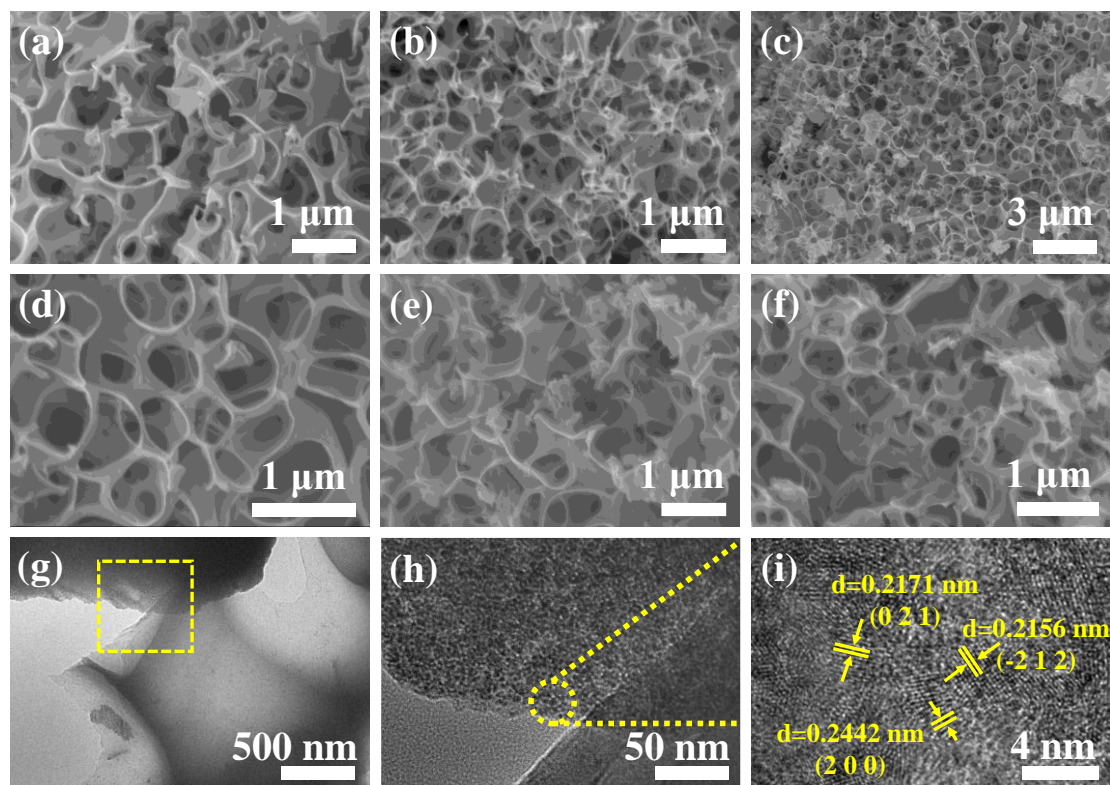


**Figure 1** SEM images of CN-MoO<sub>2</sub>-400 (a), CN-MoO<sub>2</sub>-500 (b), CN-MoO<sub>2</sub>-600 (c and d), CN-MoO<sub>2</sub>-700 (e), CN-MoO<sub>2</sub>C-800 (f); TEM images of CN-MoO<sub>2</sub>-600 (g-i).

To disclose the influence of carbonization temperature on the formation of molybdenum-based composites, a variety of characterization methods were applied. The obvious diffraction peaks situated in the  $2\theta$  of  $26.03^\circ$ ,  $37.02^\circ$ , and  $53.5^\circ$  in the XRD patterns of the CN-MoO<sub>2</sub> composites (**Figure 2a**) correspond to the (-111), (-211) and (-312) crystal planes of monoclinic MoO<sub>2</sub> (JCPDS No. 32-0671) [33]. The characteristic peaks in the samples annealed at 800 °C located at  $2\theta$  of  $34.4^\circ$ ,  $37.9^\circ$ ,  $39.5^\circ$ , were indexed to (100), (002), (101) crystal planes of Mo<sub>2</sub>C (JCPDS No. 11-0680) [34-35], which indicated the conversion of MoO<sub>2</sub> to Mo<sub>2</sub>C when the

carbonization temperature was increased to 800 °C. Besides, no other diffraction peaks were observed in Figure 2a illustrates that no impurities or by-products were generated by regulating carbonization temperatures.

To further assess the quality of carbon matrix in Mo-based composites, the Raman spectroscopy was applied. Figure 2b presents the Raman spectra of the CN-MoO<sub>2</sub> obtained at different heat treatment temperatures and CN-Mo<sub>2</sub>C samples. The observed two apparent widened peaks at approximately 1347 and 1583 cm<sup>-1</sup> were ascribed to E<sub>2g</sub> vibration mode (G-band) and A<sub>1g</sub> vibration mode (D-band) that correspond to the order and disorder graphitic carbon, respectively. The ratio of I<sub>D</sub>/I<sub>G</sub> intensity was calculated to *ca.* 0.891, 0.857, 0.842, 0.937 and 0.991 for the composites obtained with the annealed temperature ranged from 400 to 800 °C. This implies a beneficial degree of graphitization in all the prepared hybrids, which are instrumental in promoting the transmission of electrons and guarantee the efficient reactions during cycling processes. The I<sub>D</sub>/I<sub>G</sub> value showed a trend of decrease first and then increase along with the increase of carbonization temperature, and the CN-MoO<sub>2</sub>-600 composite displayed the minimum value among the samples.

The content of carbon and MoO<sub>2</sub> in CN-MoO<sub>2</sub>-600 composites was investigated by TGA analysis, Figure 2c. The incipient weight loss of 4.3 % before 200 °C was caused by residual moisture and solvent evaporation on the surface of CN-MoO<sub>2</sub>-600. The main weight loss of 23.0 % between 200 °C to 750 °C was due to the oxidation reaction of MoO<sub>2</sub> to MoO<sub>3</sub> and the combustion of the porous carbon [36]. The content of carbon and MoO<sub>2</sub> was calculated to be *ca.* 35.51 % and 64.49 %, respectively. The

high content of carbon formed the 3D porous framework, which was beneficial to relieve the volume changes of MoO<sub>2</sub> and improve the instinctive low electronic conductivity during charge/discharge process.

The N<sub>2</sub> adsorption-desorption isotherms and the corresponding BJH pore size distribution of the synthesized CN-MoO<sub>2</sub>-600 composite were exhibited in the Figure 2d and e. The curve showed a similar curve to the Type IV isotherm with a characteristic hysteresis loop, which proved the mesoporous properties of CN-MoO<sub>2</sub>-600 composite. The specific surface area of the CN-MoO<sub>2</sub>-600 sample was measured to be *ca.* 27.6 m<sup>2</sup> g<sup>-1</sup> and the average pore size was *ca.* 1.7 nm. It's worth noting that the N<sub>2</sub> adsorption and desorption curve was not closed, which may be due to the fact that the pores tend to shrink when the carbon material adsorbs gas, which makes it difficult for the adsorbed gas to desorb [37]. The mesoporous structure and relatively large specific surface area are considered to increase the contact area of electrolyte/electrodes and accommodate more active sites, resulting in excellent electrochemical properties of high capacity and super rate capability.

The surface electronic states and chemical composition of the as-prepared Mo-based composites was explored via X-ray photoelectron spectroscopy (XPS), Figure 2f-m (CN-MoO<sub>2</sub>-600) and **Figure S2-4** (CN-MoO<sub>2</sub>-400, CN-MoO<sub>2</sub>-500, and CN-MoO<sub>2</sub>-700, respectively). The distinct peaks located at *ca.* 232.59, 284.72, 398.22, and 530.58 eV in Figure 2f, correspond to Mo 3d, C 1s, N 1s and O 1s respectively. The high resolution XPS spectra of the Mo 3d in Figure 2g was divided into two doublets. One doublet at 229.6 and 233.5 eV was indexed to the Mo 3d<sub>5/2</sub> and Mo

$3d_{3/2}$  of  $\text{Mo}^{4+}$ . The doublet peaks at 232.6 and 235.8 eV belong to another group that were believed to be the  $\text{Mo } 3d_{5/2}$  and  $\text{Mo } 3d_{3/2}$  of  $\text{Mo}^{6+}$ . The existence of  $\text{Mo}^{6+}$  peaks was caused by the oxidation of  $\text{MoO}_2$  when exposing to air under high energy condition. The high resolution XPS spectra of C 1s exhibited in Figure 2h were classified into four peaks situated at 284.3, 284.8, 285.8 and 286.8 eV, which were distinguished as C=C, C-C, C=N and C-N, respectively. Meanwhile, the spectra of O 1s (Figure 2i) were distinguished into three peaks: lattice oxygen at *ca.* 529.6 eV, OH group at *ca.* 530.4 eV and adsorbed water on the surface of Mo-based hybrids at *ca.* 531.1 eV [38-41].

Furthermore, the high resolution XPS spectra of N 1s in Figure 2j-m, were chopped up into five peaks around 395.7, 398.7, 397.6, 399.4 and 400.4 eV, which correspond to  $\text{Mo } 3p_{3/2}$   $\text{Mo}^{4+}$  and  $\text{Mo}^{6+}$ , Pyridinic N, Pyrrolic N, Graphite N, respectively [15]. All the as-prepared composites were rich in nitrogen element, which was derived from the pyrolysis of urea. The nitrogen content of CN- $\text{MoO}_2$ -400, CN- $\text{MoO}_2$ -500, CN- $\text{MoO}_2$ -600, CN- $\text{MoO}_2$ -700 was examined to be *ca.* 19.42%, 21.23%, 26.38%, 19.95%, respectively. The appearance of  $\text{Mo}^{4+}$  and  $\text{Mo}^{6+}$  peaks in N 1s was ascribed to N peak partially overlaps with  $\text{Mo } 3p_{3/2}$  [15]. The results indicated that the nitrogen element was introduced into the carbon matrix in all the as-prepared composites, which was beneficial to enhance the electronic conductivity. The results also illustrated the content and composition of nitrogen was influenced by pyrolysis temperature. Pyrrolic nitrogen might be converted into graphitic and pyridinic nitrogen as the pyrolysis temperature increases and the formation of graphitic nitrogen

might offer extra free electrons to enhance electronic conductivity, promoting the improvement of electrochemical performance. The subsequent decrease in nitrogen content was because of the appearance of phase transition at higher annealed temperature [15, 36, 42-44]. It was concluded that the carbon-nitrogen composite MoO<sub>2</sub> material was successfully synthesized.

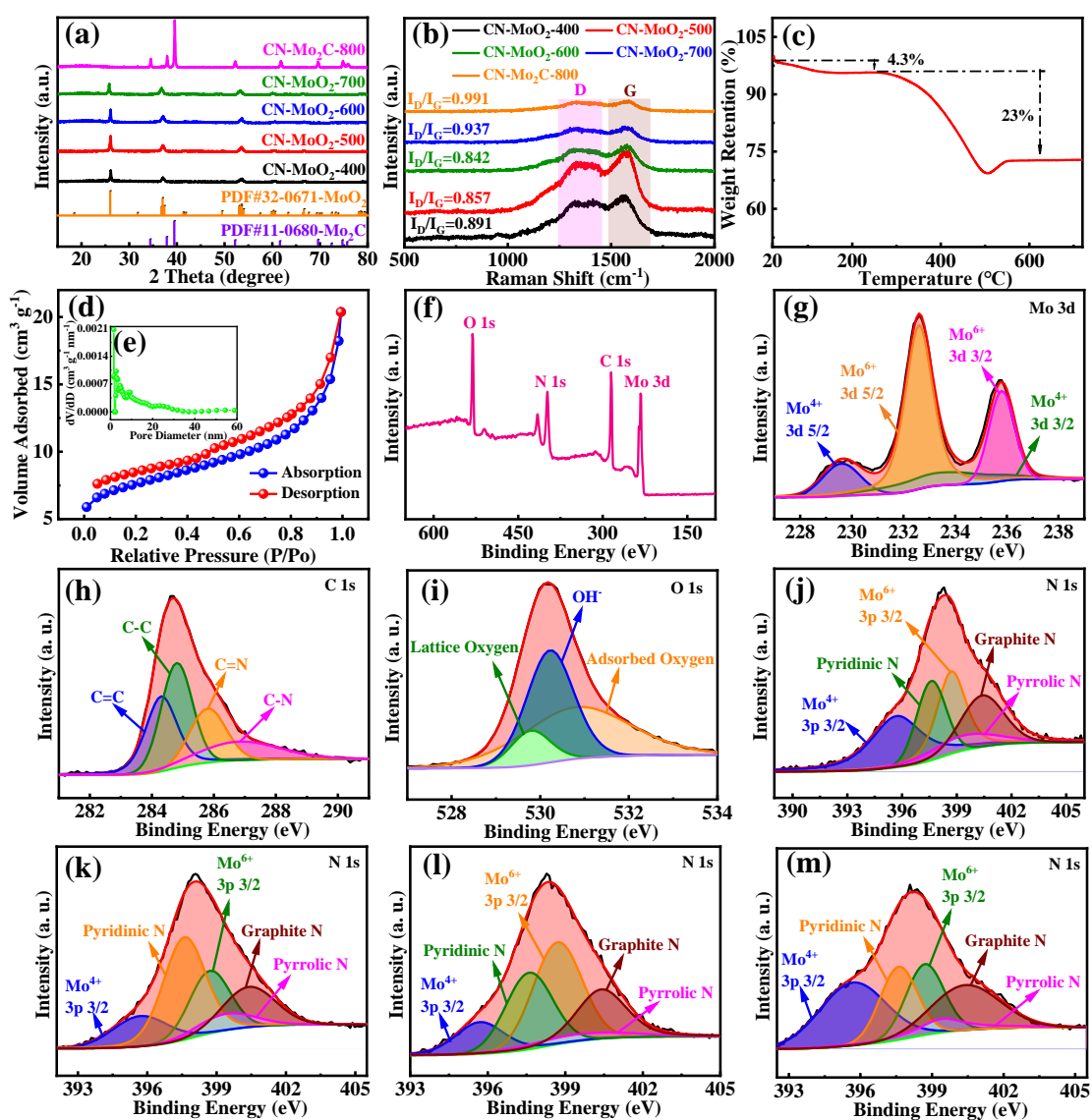


**Figure 2** (a) XRD patterns and (b) Raman spectra of CN-MoO<sub>2</sub>-400, CN-MoO<sub>2</sub>-500, CN-MoO<sub>2</sub>-600, CN-MoO<sub>2</sub>-700 and CN-Mo<sub>2</sub>C-800; TGA curves (c), N<sub>2</sub> adsorption-desorption isotherms (d) and pore size distributions (e) of CN-MoO<sub>2</sub>-600; XPS survey (f) and high resolution XPS spectra of Mo 3d (g), C 1s (h), O 1s (i), N 1s (j) of

CN-MoO<sub>2</sub>-600; high resolution XPS spectra of N 1s (k-m) of CN-MoO<sub>2</sub>-400, CN-MoO<sub>2</sub>-500, CN-MoO<sub>2</sub>-700, respectively.

The oxygen vacancy defects were introduced into the Mo-based composites during the phase transition of (NH<sub>4</sub>)<sub>6</sub>Mo<sub>7</sub>O<sub>24</sub>·4H<sub>2</sub>O to MoO<sub>2</sub> with the increase of annealing temperature. **Figure 3a-d** presents the high-resolution XPS spectra of O 1s in CN-MoO<sub>2</sub> composites, respectively. All the as-prepared composites presented the similar fitting curves of O 1s in CN-MoO<sub>2</sub>-600 composites. The OH<sup>-</sup> groups were judged to be related to the defects of oxygen vacancies among the fitting peaks according to the previously researches [32]. Figure 3e exhibits the ratio of OH<sup>-</sup> group to lattice oxygen, which qualitatively showed the content of oxygen vacancies in CN-MoO<sub>2</sub> hybrids, and certified that the relative content of oxygen vacancy was affected by temperature. For quantitative analysis the oxygen vacancies in the prepared composites, the electron paramagnetic resonance tests of CN-MoO<sub>2</sub>-500, CN-MoO<sub>2</sub>-600, CN-MoO<sub>2</sub>-700 were implemented, as shown in Figure 3f. The obvious peak with the maximum value in CN-MoO<sub>2</sub>-600 composite while the g-factor around 2.002 testified that existence of large number of oxygen vacancies in it, which agree well with the XPS results.

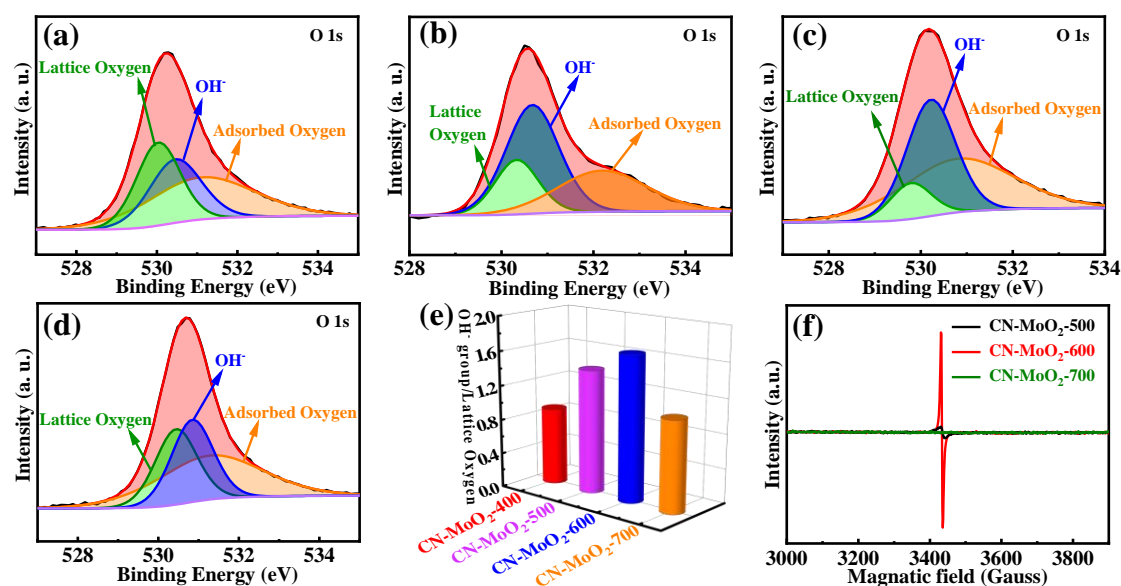


**Figure 3** Oxygen vacancies were determined by high resolution XPS spectra of O 1s in CN-MoO<sub>2</sub> hybrids annealed at 400 to 700 °C (a-d); the ratio of OH<sup>-</sup> group to lattice oxygen in the as-prepared composites (e); and electron paramagnetic resonance (EPR) tests of CN-MoO<sub>2</sub>-500, CN-MoO<sub>2</sub>-600, CN-MoO<sub>2</sub>-700 (f).

With the purpose of exploring the electrochemical performance of the prepared composite, the obtained powder materials as electrodes were assembled into half-cells.

**Figure 4a** displays the CV curves for the initial four-cycles of CN-MoO<sub>2</sub>-600 at 0.2 mV s<sup>-1</sup>. The two distinct viewed reversible reduction peaks located at 1.20/1.28 and 1.51/1.70 V during the initial cycle, illustrate the phase transition from monoclinic phase to oblique cross phase and the insertion of Li<sup>+</sup> to form the Li<sub>x</sub>MoO<sub>2</sub> orthogonal phase (0 < x < 0.98) [11,45-47]. Then the reduction peak shift slightly to the higher potential position in the subsequent cycles was on account of the continuous activation of the electrodes, which improved the reaction kinetics and the reversible phase transition reaction [16]. The peak at 0.72 V was merely caught in initial cycle because this peak represents the irreversible formation of SEI films. An inconspicuous peak situated at 0.5 V was attributed to the decomposition of Li<sub>x</sub>MoO<sub>2</sub> into Li<sub>2</sub>O and

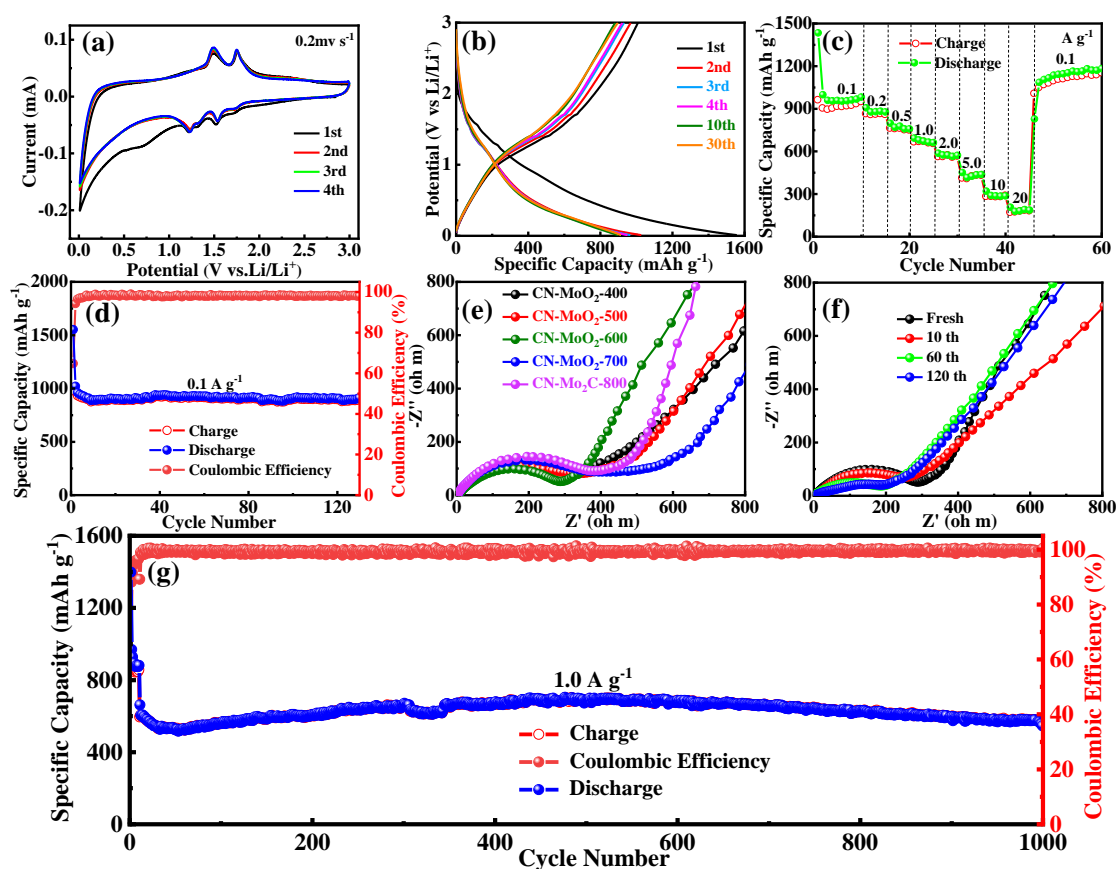
Mo [36,45-47]. The occurrence of oxidation peaks at 1.48 and 1.75 V are caused by the deintercalation of  $\text{Li}^+$  and the phase transition from the quadrature phase ( $\text{Li}_x\text{MoO}_2$ ) to the monoclinic phase ( $\text{MoO}_2$ ). The almost overlapping of CV curves of the subsequent cycles explains the excellent cycling reversibility of the CN-MoO<sub>2</sub>-600 electrodes [11, 16, 48-49]. The CV curves of other electrodes obtained under different temperature are showed in **Figure S5**, all the other MoO<sub>2</sub>-based electrodes except CN-Mo<sub>2</sub>C-800 undergoes similar redox reactions, which agrees with the XRD results.

Figure 4b displays the selected galvanostatic charge-discharge profiles of CN-MoO<sub>2</sub>-600 electrodes at 0.1 A g<sup>-1</sup>. The initial coulombic efficiency was calculated to be 64.78 % based on data originated from the initial discharge/charge capacity of 1557.2 mAh g<sup>-1</sup> and 1008.7 mAh g<sup>-1</sup>, respectively. The relatively low coulombic efficiency and capacity loss of the initial cycle were mainly ascribed to the some irreversible reactions, including the formation of SEI films and decomposition of electrolyte, et al. [11]. Satisfyingly, the charge/discharge profiles presented a high degree of overlap from the subsequent cycles, leading to the high coulomb efficiency over 98 % during subsequent cycling processes. Furthermore, the charge/discharge platform corresponded well to the CV results. The charge/discharge profiles of other electrodes obtained under different temperature are shown in **Figure S6**, where the initial coulombic efficiency was calculated to be 59.76 %, 72.91 %, 52.90 % and 44.80 %, respectively.

To further probe the electrochemical performance of CN-MoO<sub>2</sub>-600 electrodes, the rate capability was carried out and displayed in Figure 4c. The reversible capacities of *ca.* 958.82 (0.1), 877.62 (0.2), 769.96 (0.5), 680.44 (1.0), 574.78 (2.0), 415.74 (5.0), 287.00 (10.0) and 181.25 mAh g<sup>-1</sup> (20.0 A g<sup>-1</sup>) were achieved. The CN-MoO<sub>2</sub>-600 electrodes can recover to the specific capacity of *ca.*1136.25 mAh g<sup>-1</sup> when the current density was reset to 0.1 A g<sup>-1</sup> after 50 cycles under varying current density. The charge/discharge profiles corresponding to the rate performance of CN-MoO<sub>2</sub>-600 are presented in **Figure S7**, showing a typical phenomenon of voltage hysteresis, indicating excellent reaction kinetics of CN-MoO<sub>2</sub>-600. The rate capability of other prepared Mo-based composites was exhibited in **Figure S8**, presenting good capacity reversibility. **The results illustrated that the oxygen vacancies-rich CN-MoO<sub>2</sub>-600 electrodes with superior electrochemical performance were obtained thanks to the improved electronic conductivity and shortened transportation path of e<sup>-</sup> and Li<sup>+</sup>.**

The cycling performance of the prepared CN-MoO<sub>2</sub>-600 electrodes was examined at 0.1 and 1.0 A g<sup>-1</sup> in Figure 4d&g. A satisfactory capacity of 918.2 mAh g<sup>-1</sup> after 130 cycles at 0.1 A g<sup>-1</sup> was obtained, which is beyond its theoretical specific capacity without obvious capacity changes with the high coulombic efficiency over 98.1 %. The reversible capacities of 769.7, 806.1, 615.7 and 372.1 mAh g<sup>-1</sup> of CN-MoO<sub>2</sub>-400, CN-MoO<sub>2</sub>-500, CN-MoO<sub>2</sub>-700 and CN-Mo<sub>2</sub>C-800 electrodes after 100 cycles at 0.1 A g<sup>-1</sup>, as shown in **Figure S9**, indicate that the CN-MoO<sub>2</sub>-600 electrodes exhibited the highest cycling stability performance. The cycling performance of CN-MoO<sub>2</sub>-600

electrodes was also tested at  $1.0 \text{ A g}^{-1}$  in Figure 4g. The CN-MoO<sub>2</sub>-600 electrodes display exceptional stable cycling lifespan with the pleasant capacity of  $562.1 \text{ mAh g}^{-1}$  and high coulomb efficiency over  $99.91 \%$  after 1000 cycles. The unique engineered 3D porous N-doped carbon matrix was believed to contribute to the outstanding cycling performance by restricting the huge volumetric changes of active electrodes during charge/discharge processes.



**Figure 4** Electrochemical performances of CN-MoO<sub>2</sub>-600 electrodes: (a) CV curves at  $0.2 \text{ mV s}^{-1}$ ; (b) The discharge/charge profiles at  $0.1 \text{ A g}^{-1}$ ; (c) rate capacities at  $0.1\text{-}20.0 \text{ A g}^{-1}$ ; (d) cycling performances at  $0.1 \text{ A g}^{-1}$ ; (e) Nyquist plots of Mo-based composites; (f) Nyquist plots of CN-MoO<sub>2</sub>-600 samples under different cycles; (g) long lifespan cycling performance at  $1.0 \text{ A g}^{-1}$ .

The cycling performance in Figure 4g shows the capacity changes phenomenon that initial capacity declines and subsequent capacity increases. Capacity changes in

TMOs electrodes are the common phenomenon that may be caused by multi-reasons. First, the decrease of capacity would be attribute to the instability of SEI layer and the partial degradation of electrolyte. Then, the increase of the capacity would be produced by the full infiltration of electrolyte and the continuous activation of MoO<sub>2</sub> nanoparticles in 3D porous carbon matrix. Furthermore, the gel-like film on the surface of active materials with high electrochemical activity contributes to certain capacity. Besides, the distinctive 3D structure with oxygen vacancy and the introduction of heterogeneous element in carbon matrix enhanced the capacitance contribution [7, 12].

The electrochemical impedance spectroscopy (EIS) of Mo-based electrodes is shown in Figure 4e. The Nyquist plots consists of a semicircle (high-frequency region) and slop line (low-frequency region). The CN-MoO<sub>2</sub>-600 electrodes exhibit a lower electron transfer resistance and a greater slope, indicating a lower diffusion resistance to promote transfer of e<sup>-</sup>. The EIS curves of CN-MoO<sub>2</sub>-600 electrodes after different cycles are shown in Figure 4f. The impedance value of CN-MoO<sub>2</sub>-600 electrode became smaller gradually, explaining the uninterrupted activations of the CN-MoO<sub>2</sub>-600 electrodes at charging-discharging runs and final reach steady-state.

For discovering the composition mechanism of the obtained capacity, the kinetics of the CN-MoO<sub>2</sub>-600 electrodes was explored (**Figure 5**). The CV tests of the CN-MoO<sub>2</sub>-600 electrodes were put into effect at variable scan rates between 0.1-1.5 mV s<sup>-1</sup>, as shown in Figure 5a. Mild voltage delay phenomenon with the increase of scan rates is observed, which illustrated the transmission rate of Li<sup>+</sup> and e<sup>-</sup> are

effectively promoted by the 3D porous N-doped structure and introduced oxygen vacancies. The storage mechanism was further examined by probing into the correlation between scan rate ( $v$ ) and current ( $i$ ), basing on eqns (3, 4) [50]:

$$i = av^b \quad (3)$$

$$\log i = b \log v + \log a \quad (4)$$

where  $a$ ,  $b$  is constant achieved through eqn (3). Generally, the storage behaviors can be divided into two forms, including surface charge transfer that generates capacitance contribution and lithiation/delithiation-reaction that generates diffusion contribution [11, 51-52], which were determined by the  $b$ -value from eqn (3), where the  $b$ -value approach 0.5 (1.0) signified the diffusion contribution (capacitance contribution) dominates foreground. The fitting calculation results of the  $b$  value floated between 0.63 and 0.87 (Figure 5d) based on the fitting calculation (Figure 5b and c), showing the total capacity roots in the synergetic contribution of the two forms.

The precise ratio of the two forms capacity contribution was further calculated via eqns (5, 6) [53]:

$$i = k_1v + k_2v^{1/2} \quad (5)$$

$$i/v^{1/2} = k_1v^{1/2} + k_2 \quad (6)$$

where  $k_1$  and  $k_2$  are constant achieved through eqn (5),  $k_1v$  on behalf of diffusion contribution and  $k_2v^{1/2}$  means the capacitance contribution. The fitting profiles between  $v^{1/2}$  and  $i/v^{1/2}$  are displayed in **Figure S10**. The capacitance contribution of CN-MoO<sub>2</sub>-600 electrodes was calculated to be *ca.* 40.88 %, 50.36 %, 55.64 %, 59.88 %, 64.12 %, 68.36 %, 72.60 %, 76.84 %, 81.08 %, 85.32 %, 89.56 %, 93.80 %, 98.04 %, 102.28 %, 106.52 %, 110.76 %, 115.00 %, 119.24 %, 123.48 %, 127.72 %, 131.96 %, 136.20 %, 140.44 %, 144.68 %, 148.92 %, 153.16 %, 157.40 %, 161.64 %, 165.88 %, 170.12 %, 174.36 %, 178.60 %, 182.84 %, 187.08 %, 191.32 %, 195.56 %, 199.80 %, 204.04 %, 208.28 %, 212.52 %, 216.76 %, 221.00 %, 225.24 %, 229.48 %, 233.72 %, 237.96 %, 242.20 %, 246.44 %, 250.68 %, 254.92 %, 259.16 %, 263.40 %, 267.64 %, 271.88 %, 276.12 %, 280.36 %, 284.60 %, 288.84 %, 293.08 %, 297.32 %, 301.56 %, 305.80 %, 310.04 %, 314.28 %, 318.52 %, 322.76 %, 327.00 %, 331.24 %, 335.48 %, 339.72 %, 343.96 %, 348.20 %, 352.44 %, 356.68 %, 360.92 %, 365.16 %, 369.40 %, 373.64 %, 377.88 %, 382.12 %, 386.36 %, 390.60 %, 394.84 %, 399.08 %, 403.32 %, 407.56 %, 411.80 %, 416.04 %, 420.28 %, 424.52 %, 428.76 %, 433.00 %, 437.24 %, 441.48 %, 445.72 %, 450.00 %, 454.24 %, 458.48 %, 462.72 %, 466.96 %, 471.20 %, 475.44 %, 479.68 %, 483.92 %, 488.16 %, 492.40 %, 496.64 %, 500.88 %, 505.12 %, 509.36 %, 513.60 %, 517.84 %, 522.08 %, 526.32 %, 530.56 %, 534.80 %, 539.04 %, 543.28 %, 547.52 %, 551.76 %, 556.00 %, 560.24 %, 564.48 %, 568.72 %, 572.96 %, 577.20 %, 581.44 %, 585.68 %, 589.92 %, 594.16 %, 598.40 %, 602.64 %, 606.88 %, 611.12 %, 615.36 %, 619.60 %, 623.84 %, 628.08 %, 632.32 %, 636.56 %, 640.80 %, 645.04 %, 649.28 %, 653.52 %, 657.76 %, 662.00 %, 666.24 %, 670.48 %, 674.72 %, 678.96 %, 683.20 %, 687.44 %, 691.68 %, 695.92 %, 700.16 %, 704.40 %, 708.64 %, 712.88 %, 717.12 %, 721.36 %, 725.60 %, 729.84 %, 734.08 %, 738.32 %, 742.56 %, 746.80 %, 751.04 %, 755.28 %, 759.52 %, 763.76 %, 768.00 %, 772.24 %, 776.48 %, 780.72 %, 784.96 %, 789.20 %, 793.44 %, 797.68 %, 801.92 %, 806.16 %, 810.40 %, 814.64 %, 818.88 %, 823.12 %, 827.36 %, 831.60 %, 835.84 %, 840.08 %, 844.32 %, 848.56 %, 852.80 %, 857.04 %, 861.28 %, 865.52 %, 869.76 %, 874.00 %, 878.24 %, 882.48 %, 886.72 %, 890.96 %, 895.20 %, 899.44 %, 903.68 %, 907.92 %, 912.16 %, 916.40 %, 920.64 %, 924.88 %, 929.12 %, 933.36 %, 937.60 %, 941.84 %, 946.08 %, 950.32 %, 954.56 %, 958.80 %, 963.04 %, 967.28 %, 971.52 %, 975.76 %, 980.00 %, 984.24 %, 988.48 %, 992.72 %, 996.96 %, 1001.20 %, 1005.44 %, 1009.68 %, 1013.92 %, 1018.16 %, 1022.40 %, 1026.64 %, 1030.88 %, 1035.12 %, 1039.36 %, 1043.60 %, 1047.84 %, 1052.08 %, 1056.32 %, 1060.56 %, 1064.80 %, 1069.04 %, 1073.28 %, 1077.52 %, 1081.76 %, 1086.00 %, 1090.24 %, 1094.48 %, 1098.72 %, 1102.96 %, 1107.20 %, 1111.44 %, 1115.68 %, 1119.92 %, 1124.16 %, 1128.40 %, 1132.64 %, 1136.88 %, 1141.12 %, 1145.36 %, 1149.60 %, 1153.84 %, 1158.08 %, 1162.32 %, 1166.56 %, 1170.80 %, 1175.04 %, 1179.28 %, 1183.52 %, 1187.76 %, 1192.00 %, 1196.24 %, 1200.48 %, 1204.72 %, 1208.96 %, 1213.20 %, 1217.44 %, 1221.68 %, 1225.92 %, 1230.16 %, 1234.40 %, 1238.64 %, 1242.88 %, 1247.12 %, 1251.36 %, 1255.60 %, 1259.84 %, 1264.08 %, 1268.32 %, 1272.56 %, 1276.80 %, 1281.04 %, 1285.28 %, 1289.52 %, 1293.76 %, 1298.00 %, 1302.24 %, 1306.48 %, 1310.72 %, 1314.96 %, 1319.20 %, 1323.44 %, 1327.68 %, 1331.92 %, 1336.16 %, 1340.40 %, 1344.64 %, 1348.88 %, 1353.12 %, 1357.36 %, 1361.60 %, 1365.84 %, 1370.08 %, 1374.32 %, 1378.56 %, 1382.80 %, 1387.04 %, 1391.28 %, 1395.52 %, 1399.76 %, 1404.00 %, 1408.24 %, 1412.48 %, 1416.72 %, 1420.96 %, 1425.20 %, 1429.44 %, 1433.68 %, 1437.92 %, 1442.16 %, 1446.40 %, 1450.64 %, 1454.88 %, 1459.12 %, 1463.36 %, 1467.60 %, 1471.84 %, 1476.08 %, 1480.32 %, 1484.56 %, 1488.80 %, 1493.04 %, 1497.28 %, 1501.52 %, 1505.76 %, 1510.00 %, 1514.24 %, 1518.48 %, 1522.72 %, 1526.96 %, 1531.20 %, 1535.44 %, 1539.68 %, 1543.92 %, 1548.16 %, 1552.40 %, 1556.64 %, 1560.88 %, 1565.12 %, 1569.36 %, 1573.60 %, 1577.84 %, 1582.08 %, 1586.32 %, 1590.56 %, 1594.80 %, 1599.04 %, 1603.28 %, 1607.52 %, 1611.76 %, 1616.00 %, 1620.24 %, 1624.48 %, 1628.72 %, 1632.96 %, 1637.20 %, 1641.44 %, 1645.68 %, 1649.92 %, 1654.16 %, 1658.40 %, 1662.64 %, 1666.88 %, 1671.12 %, 1675.36 %, 1679.60 %, 1683.84 %, 1688.08 %, 1692.32 %, 1696.56 %, 1700.80 %, 1705.04 %, 1709.28 %, 1713.52 %, 1717.76 %, 1722.00 %, 1726.24 %, 1730.48 %, 1734.72 %, 1738.96 %, 1743.20 %, 1747.44 %, 1751.68 %, 1755.92 %, 1760.16 %, 1764.40 %, 1768.64 %, 1772.88 %, 1777.12 %, 1781.36 %, 1785.60 %, 1789.84 %, 1794.08 %, 1798.32 %, 1802.56 %, 1806.80 %, 1811.04 %, 1815.28 %, 1819.52 %, 1823.76 %, 1828.00 %, 1832.24 %, 1836.48 %, 1840.72 %, 1844.96 %, 1849.20 %, 1853.44 %, 1857.68 %, 1861.92 %, 1866.16 %, 1870.40 %, 1874.64 %, 1878.88 %, 1883.12 %, 1887.36 %, 1891.60 %, 1895.84 %, 1900.08 %, 1904.32 %, 1908.56 %, 1912.80 %, 1917.04 %, 1921.28 %, 1925.52 %, 1929.76 %, 1934.00 %, 1938.24 %, 1942.48 %, 1946.72 %, 1950.96 %, 1955.20 %, 1959.44 %, 1963.68 %, 1967.92 %, 1972.16 %, 1976.40 %, 1980.64 %, 1984.88 %, 1989.12 %, 1993.36 %, 1997.60 %, 2001.84 %, 2006.08 %, 2010.32 %, 2014.56 %, 2018.80 %, 2023.04 %, 2027.28 %, 2031.52 %, 2035.76 %, 2040.00 %, 2044.24 %, 2048.48 %, 2052.72 %, 2056.96 %, 2061.20 %, 2065.44 %, 2069.68 %, 2073.92 %, 2078.16 %, 2082.40 %, 2086.64 %, 2090.88 %, 2095.12 %, 2099.36 %, 2103.60 %, 2107.84 %, 2112.08 %, 2116.32 %, 2120.56 %, 2124.80 %, 2129.04 %, 2133.28 %, 2137.52 %, 2141.76 %, 2146.00 %, 2150.24 %, 2154.48 %, 2158.72 %, 2162.96 %, 2167.20 %, 2171.44 %, 2175.68 %, 2179.92 %, 2184.16 %, 2188.40 %, 2192.64 %, 2196.88 %, 2201.12 %, 2205.36 %, 2209.60 %, 2213.84 %, 2218.08 %, 2222.32 %, 2226.56 %, 2230.80 %, 2235.04 %, 2239.28 %, 2243.52 %, 2247.76 %, 2252.00 %, 2256.24 %, 2260.48 %, 2264.72 %, 2268.96 %, 2273.20 %, 2277.44 %, 2281.68 %, 2285.92 %, 2290.16 %, 2294.40 %, 2298.64 %, 2302.88 %, 2307.12 %, 2311.36 %, 2315.60 %, 2319.84 %, 2324.08 %, 2328.32 %, 2332.56 %, 2336.80 %, 2341.04 %, 2345.28 %, 2349.52 %, 2353.76 %, 2358.00 %, 2362.24 %, 2366.48 %, 2370.72 %, 2374.96 %, 2379.20 %, 2383.44 %, 2387.68 %, 2391.92 %, 2396.16 %, 2400.40 %, 2404.64 %, 2408.88 %, 2413.12 %, 2417.36 %, 2421.60 %, 2425.84 %, 2430.08 %, 2434.32 %, 2438.56 %, 2442.80 %, 2447.04 %, 2451.28 %, 2455.52 %, 2459.76 %, 2464.00 %, 2468.24 %, 2472.48 %, 2476.72 %, 2480.96 %, 2485.20 %, 2489.44 %, 2493.68 %, 2497.92 %, 2502.16 %, 2506.40 %, 2510.64 %, 2514.88 %, 2519.12 %, 2523.36 %, 2527.60 %, 2531.84 %, 2536.08 %, 2540.32 %, 2544.56 %, 2548.80 %, 2553.04 %, 2557.28 %, 2561.52 %, 2565.76 %, 2570.00 %, 2574.24 %, 2578.48 %, 2582.72 %, 2586.96 %, 2591.20 %, 2595.44 %, 2599.68 %, 2603.92 %, 2608.16 %, 2612.40 %, 2616.64 %, 2620.88 %, 2625.12 %, 2629.36 %, 2633.60 %, 2637.84 %, 2642.08 %, 2646.32 %, 2650.56 %, 2654.80 %, 2659.04 %, 2663.28 %, 2667.52 %, 2671.76 %, 2676.00 %, 2680.24 %, 2684.48 %, 2688.72 %, 2692.96 %, 2697.20 %, 2701.44 %, 2705.68 %, 2709.92 %, 2714.16 %, 2718.40 %, 2722.64 %, 2726.88 %, 2731.12 %, 2735.36 %, 2739.60 %, 2743.84 %, 2748.08 %, 2752.32 %, 2756.56 %, 2760.80 %, 2765.04 %, 2769.28 %, 2773.52 %, 2777.76 %, 2782.00 %, 2786.24 %, 2790.48 %, 2794.72 %, 2798.96 %, 2803.20 %, 2807.44 %, 2811.68 %, 2815.92 %, 2820.16 %, 2824.40 %, 2828.64 %, 2832.88 %, 2837.12 %, 2841.36 %, 2845.60 %, 2849.84 %, 2854.08 %, 2858.32 %, 2862.56 %, 2866.80 %, 2871.04 %, 2875.28 %, 2879.52 %, 2883.76 %, 2888.00 %, 2892.24 %, 2896.48 %, 2900.72 %, 2904.96 %, 2909.20 %, 2913.44 %, 2917.68 %, 2921.92 %, 2926.16 %, 2930.40 %, 2934.64 %, 2938.88 %, 2943.12 %, 2947.36 %, 2951.60 %, 2955.84 %, 2960.08 %, 2964.32 %, 2968.56 %, 2972.80 %, 2977.04 %, 2981.28 %, 2985.52 %, 2989.76 %, 2994.00 %, 2998.24 %, 3002.48 %, 3006.72 %, 3010.96 %, 3015.20 %, 3019.44 %, 3023.68 %, 3027.92 %, 3032.16 %, 3036.40 %, 3040.64 %, 3044.88 %, 3049.12 %, 3053.36 %, 3057.60 %, 3061.84 %, 3066.08 %, 3070.32 %, 3074.56 %, 3078.80 %, 3083.04 %, 3087.28 %, 3091.52 %, 3095.76 %, 3100.00 %, 3104.24 %, 3108.48 %, 3112.72 %, 3116.96 %, 3121.20 %, 3125.44 %, 3129.68 %, 3133.92 %, 3138.16 %, 3142.40 %, 3146.64 %, 3150.88 %, 3155.12 %, 3159.36 %, 3163.60 %, 3167.84 %, 3172.08 %, 3176.32 %, 3180.56 %, 3184.80 %, 3189.04 %, 3193.28 %, 3197.52 %, 3201.76 %, 3206.00 %, 3210.24 %, 3214.48 %, 3218.72 %, 3222.96 %, 3227.20 %, 3231.44 %, 3235.68 %, 3239.92 %, 3244.16 %, 3248.40 %, 3252.64 %, 3256.88 %, 3261.12 %, 3265.36 %, 3269.60 %, 3273.84 %, 3278.08 %, 3282.32 %, 3286.56 %, 3290.80 %, 3295.04 %, 3299.28 %, 3303.52 %, 3307.76 %, 3312.00 %, 3316.24 %, 3320.48 %, 3324.72 %, 3328.96 %, 3333.20 %, 3337.44 %, 3341.68 %, 3345.92 %, 3350.16 %, 3354.40 %, 3358.64 %, 3362.88 %, 3367.12 %, 3371.36 %, 3375.60 %, 3379.84 %, 3384.08 %, 3388.32 %, 3392.56 %, 3396.80 %, 3401.04 %, 3405.28 %, 3409.52 %, 3413.76 %, 3418.00 %, 3422.24 %, 3426.48 %, 3430.72 %, 3434.96 %, 3439.20 %, 3443.44 %, 3447.68 %, 3451.92 %, 3456.16 %, 3460.40 %, 3464.64 %, 3468.88 %, 3473.12 %, 3477.36 %, 3481.60 %, 3485.84 %, 3490.08 %, 3494.32 %, 3498.56 %, 3502.80 %, 3507.04 %, 3511.28 %, 3515.52 %, 3519.76 %, 3524.00 %, 3528.24 %, 3532.48 %, 3536.72 %, 3540.96 %, 3545.20 %, 3549.44 %, 3553.68 %, 3557.92 %, 3562.16 %, 3566.40 %, 3570.64 %, 3574.88 %, 3579.12 %, 3583.36 %, 3587.60 %, 3591.84 %, 3596.08 %, 3600.32 %, 3604.56 %, 3608.80 %, 3613.04 %, 3617.28 %, 3621.52 %, 3625.76 %, 3630.00 %, 3634.24 %, 3638.48 %, 3642.72 %, 3646.96 %, 3651.20 %, 3655.44 %, 3659.68 %, 3663.92 %, 3668.16 %, 3672.40 %, 3676.64 %, 3680.88 %, 3685.12 %, 3689.36 %, 3693.60 %, 3697.84 %, 3702.08 %, 3706.32 %, 3710.56 %, 3714.80 %, 3719.04 %, 3723.28 %, 3727.52 %, 3731.76 %, 3736.00 %, 3740.24 %, 3744.48 %, 3748.72 %, 3752.96 %, 3757.20 %, 3761.44 %, 3765.68 %, 3769.92 %, 3774.16 %, 3778.40 %, 3782.64 %, 3786.88 %, 3791.12 %, 3795.36 %, 3799.60 %, 3803.84 %, 3808.08 %, 3812.32 %, 3816.56 %, 3820.80 %, 3825.04 %, 3829.28 %, 3833.52 %, 3837.76 %, 3842.00 %, 3846.24 %, 3850.48 %, 3854.72 %, 3858.96 %, 3863.20 %, 3867.44 %, 3871.68 %, 3875.92 %, 3880.16 %, 3884.40 %, 3888.64 %, 3892.88 %, 3897.12 %, 3901.36 %, 3905.60 %, 3909.84 %, 3914.08 %, 3918.32 %, 3922.56 %, 3926.80 %, 3931.04 %, 3935.28 %, 3939.52 %, 3943.76 %, 3948.00 %, 3952.24 %, 3956.48 %, 3960.72 %, 3964.96 %, 3969.20 %, 3973.44 %, 3977.68 %, 3981.92 %, 3986.16 %, 3990.40 %, 3994.64 %, 3998.88 %, 4003.12 %, 4007.36 %, 4011.60 %, 4015.84 %, 4020.08 %, 4024.32 %, 4028.56 %, 4032.80 %, 4037.04 %, 4041.28 %, 4045.52 %, 4049.76 %, 4054.00 %, 4058.24 %, 4062.48 %, 4066.72 %, 4070.96 %, 4075.20 %, 4079.44 %, 4083.68 %, 4087.92 %, 4092.16 %, 4096.40 %, 4100.64 %, 4104.88 %, 4109.12 %, 4113.36 %, 4117.60 %, 4121.84 %, 4126.08 %, 4130.32 %, 4134.56 %, 4138.80 %, 4143.04 %, 4147.28 %, 4151.52 %, 4155.76 %, 4160.00 %, 4164.24 %, 4168.48 %, 4172.72 %, 4176.96 %, 4181.20 %, 4185.44 %, 4189.68 %, 4193.92 %, 4198.16 %, 4202.40 %, 4206.64 %, 4210.88 %, 4215.12 %, 4219.36 %, 4223.60 %, 4227.84 %, 4232.08 %, 4236.32 %, 4240.56 %, 4244.80 %, 4249.04 %, 4253.28 %, 4257.52 %, 4261.76 %, 4266.00 %, 4270.24 %, 4274.48 %, 4278.72 %, 4282.96 %, 4287.20 %, 4291.44 %, 4295.68 %, 4300.00 %, 4304.24 %, 4308.48 %, 4312.72 %, 4316.96 %, 4321.20 %, 4325.44 %, 4329.68 %, 4333.92 %, 4338.16 %, 4342.40 %, 4346.64 %, 4350.88 %, 4355.12 %, 4359.36 %, 4363.60 %, 4367.84 %, 4372.08 %, 4376.32 %, 4380.56 %, 4384.80 %, 4389.04 %, 4393.28 %, 4397.52 %, 4401.76 %, 4406.00 %, 4410.24 %, 4414.48 %, 4418.72 %, 4422.96 %, 4427.20 %, 4431.44 %, 4435.68 %, 4439.92 %, 4444.16 %, 4448.40 %, 4452.64 %, 4456.88 %, 4461.12 %, 4465.36 %, 4469.60 %, 4473.84 %, 4478.08 %, 4482.32 %, 4486.56 %, 4490.80 %, 4495.04 %, 4499.28 %, 4503.52 %, 4507.76 %, 4512.00 %, 4516.24 %, 4520.48 %, 4524.72 %, 4528.96 %, 4533.20 %, 4537.44 %, 4541.68 %, 4545.92 %, 4550.16 %, 4554.40 %, 4558.64 %, 4562.88 %, 4567.12 %, 4571.36 %, 4575.60 %, 4579.84 %, 4584.08 %, 4588.32 %, 4592.56 %, 4596.80 %, 4601.04 %, 4605.28 %, 4609.52 %, 4613.76 %, 4618.00 %, 4622.24 %, 4626.48 %, 4630.72 %, 4634.96 %, 4639.20 %, 4643.44 %, 4647.68 %, 4651.92 %, 4656.16 %, 4660.40 %, 4664.64 %, 4668.88 %, 4673.12 %, 4677.36 %, 4681.60 %, 4685.84 %, 4690.08 %, 4694.32 %, 4698.56 %, 4702.80 %, 4707.04 %, 4711.28 %, 4715.52 %, 4719.76 %, 4724.00 %, 4728.24 %, 4732.48 %, 4736.72 %, 4740.96 %, 4745.20 %, 4749.44 %, 4753.68 %, 4757.92 %, 4762.16 %, 4766.40 %, 4770.64 %, 4774.88 %, 4779.12 %, 4783.36 %, 4787.60 %, 4791.84 %, 4796.08 %, 4800.32 %, 4804.56 %, 4808.80 %, 4813.04 %, 4817.28 %, 4821.52 %, 4825.76 %, 4830.00 %, 4834.24 %, 4838.48 %, 4842.72 %, 4846.96 %, 4851.20 %, 4855.44 %, 4859.68 %, 4863.92 %, 4868.16 %, 4872.40 %, 4876.64 %, 4880.88 %, 4885.12 %, 4889.36 %, 4893.60 %, 4897.84 %, 4902.08 %, 4906.32 %, 4910.56 %, 4914.80 %, 4919.04 %, 4923.28 %, 4927.52 %, 4931.76 %, 4936.00 %, 4940.24 %, 4944.48 %, 4948.72 %, 4952.96 %, 4957.20 %, 4961.44 %, 4965.68 %, 4969.92 %, 4974.16 %, 4978.40 %, 4982.64 %, 4986.88 %, 4991.12 %, 4995.36 %, 4999.60 %, 5003.84 %, 5008.08 %, 5012.32 %, 5016.56 %, 5020.80 %, 5025.04 %, 5029.28 %, 5033.52 %, 5037.76 %, 5042.00 %, 5046.24 %, 5050.48 %, 5054.72 %, 5058.96 %, 5063.20 %, 5067.44 %, 5071.68 %, 5075.92 %, 5080.16 %, 5084.40 %, 5088.64 %, 5092.88 %, 5097.12 %, 5101.36 %, 5105.60 %, 5109.84 %, 5114.08 %, 5118.32 %, 5122.56 %, 5126.80 %, 5131.04 %, 5135.28 %, 5139.52 %, 5143.76 %, 5148.00 %, 5152.24 %, 5156.48 %, 5160.72 %, 5164.96 %, 5169.20 %, 5173.44 %, 5177.68 %, 5181.92 %, 5186.16 %, 5190.40 %, 5194.64 %, 5198.88 %, 5203.12 %, 5207.36 %, 5211.60 %, 5215.84 %, 5220.08 %, 5224.32 %, 5228.56 %, 5232.80 %, 5237.04 %, 5241.28 %, 5245.52 %, 5249.76 %, 5254.00 %, 5258.24 %, 5262.48 %, 5266.72 %, 5270.96 %, 5275.20 %, 5279.44 %, 5283.68 %, 5287.92 %, 5292.16 %, 5296.40 %, 5300.64 %, 5304.88 %, 5309.12 %, 5313.36 %, 5317.60 %, 5321.84 %, 5326.08 %, 5330.32 %, 5334.56 %, 5338.80 %, 5343.04 %, 5347.28 %, 5351.52 %, 5355.76 %, 5360.00 %, 5364.24 %, 5368.48 %, 5372.72 %, 5376.96 %, 5381.20 %, 5385.44 %, 5389.68 %, 5393.92 %, 5398.16 %, 5402.40 %, 5406.64 %, 5410.88 %, 5415.12 %, 5419.36 %, 5423.60 %, 5427.84 %, 5432.08 %, 5436.32 %, 5440.56 %, 5444.80 %, 5449.04 %, 5453.28 %, 5457.52 %, 5461.76 %, 5466.00 %, 5470.24 %, 5474.48 %, 5478.72 %, 5482.96 %, 5487.20 %, 5491.44 %, 5495.68 %, 5500.00 %.

64.55 % and 72.73 % of total capacity at 0.1-1.5  $\text{mV s}^{-1}$  in Figure 5e, indicating the synchronous increase of capacitance contribution and scan rates. A 55.64 % of the total capacity originated from capacitance contribution is obtained at 0.5  $\text{mV s}^{-1}$  (Figure 5f). The high ratio of capacitance contribution was caused by the enhanced transportation of ions and electrons through the unique 3D porous N-doped carbon matrix and local built-in electric field derived by oxygen vacancies of CN-MoO<sub>2</sub>-600 electrodes, resulting in the obtained practical capacity beyond the theoretical specific capacity.

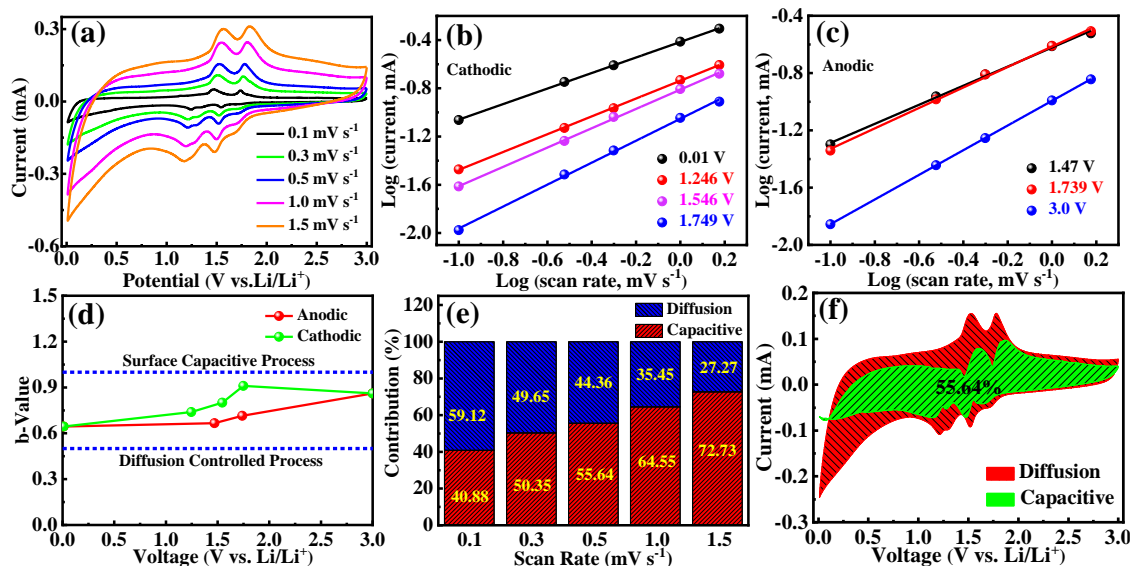


**Figure 5** Kinetics analysis of the CN-MoO<sub>2</sub>-600 electrodes: (a) CV curves at different scan rates; (b) fitting curves (current responses plotted vs scan rates) at different potentials for cathodic and (c) anodic scans; (d) b-values; (e) ratio of diffusion contribution in total storage under different scan rates; (f) the ratio of diffusion contribution at 0.5  $\text{mV s}^{-1}$ .

The previous studies of MoO<sub>2</sub>-based composites as anode electrodes for LIBs are summarized and listed in **Table 1**. The CN-MoO<sub>2</sub>-600 electrodes show superior electrochemical performance compared with most of the previous similar works,

which should be attributed to multifactor, including distinctive conceived and stability structure, delicate chemical composition, particle diameter, crystallinity, and the introduced oxygen vacancy defects. The MoO<sub>2</sub> nanoparticles anchored into the 3D porous honeycomb-like carbon matrix efficiently shortened the transfer route of ions and electrons, supplied sufficient space to mitigate volumetric changes of MoO<sub>2</sub> actives during cycling, improved the number of active sites, and enlarged contact area between MoO<sub>2</sub> electrodes and electrolyte. Equally important, the introduction of oxygen vacancy defects and their concentration control played an extremely significant part in enhancing the electrochemical performance of the prepared electrodes, which was proved by the Schematic illustration (**Figure 6a**) and the electron density difference calculation results (Figure 6b, c and e). The local built-in electric field was formed based on the emergence of oxygen vacancies, where an enriched positively charged region in the centers of oxygen vacancies, and a negatively charged region with equal charges surrounds the oxygen vacancy. Particularly, the Coulomb force stemmed from the electric field that from perfect crystal region points to negatively charged region efficiently facilitates the movement of Li<sup>+</sup> and accumulated in the negatively charged region during discharge process. The negatively charged region gradually inclined to be electrically neutral after lithiation to some extent. Then, the Coulomb force originated from the electric field pointing to electrically neutral region from centers of oxygen vacancies sped up the transmission speed of Li<sup>+</sup> during charge process. The electrochemical performance, especially the rate capability, of the CN-MoO<sub>2</sub>-600 electrodes was further improved by the

above-mentioned built-in electric field. Besides, the inherent conductivity and the number of active sites were also tremendously enhanced by the existence of oxygen vacancies, which was instrumental in obtaining excellent lithium storage behaviors, and was identified by the density of states calculation (Figure 6d).

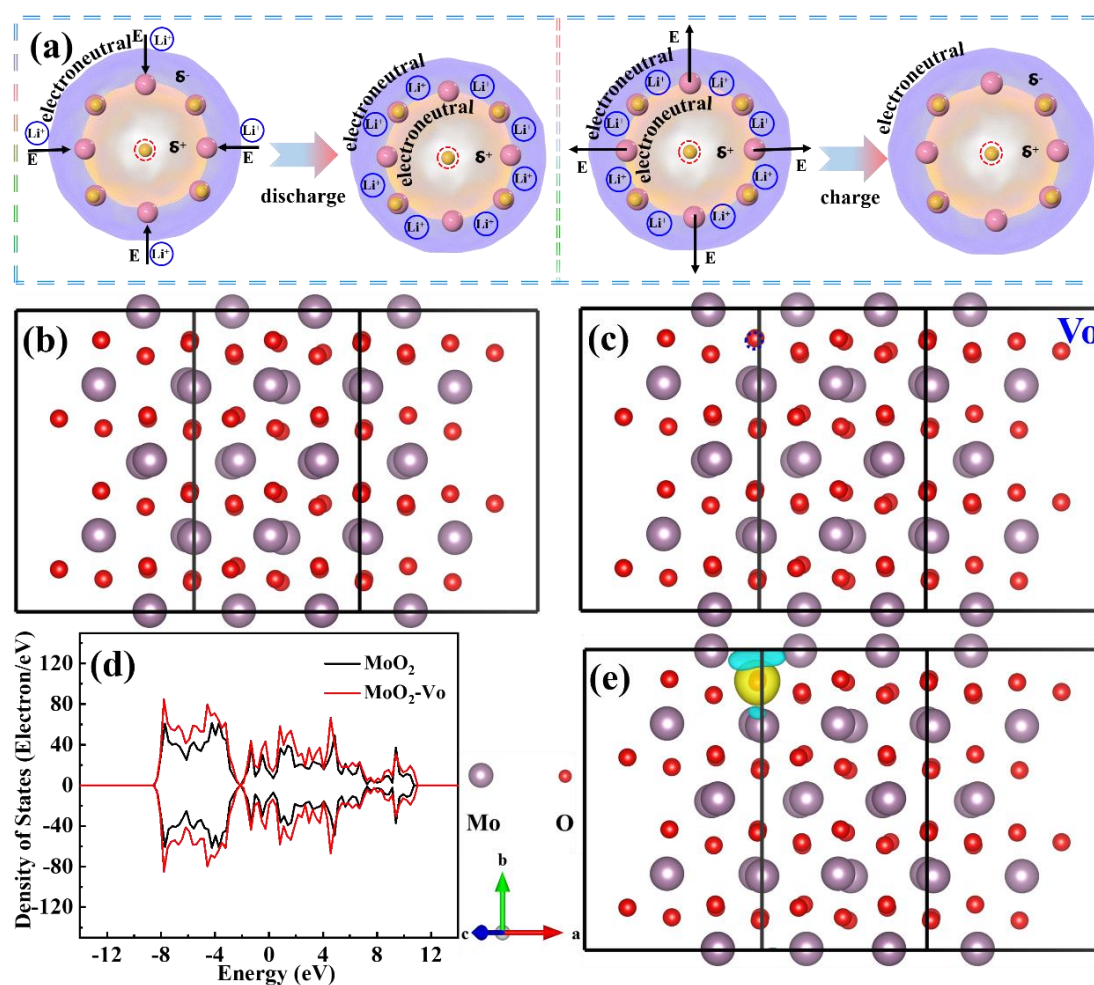


**Figure 6** (a) schematic illustration of the promoted Li<sup>+</sup> migration in crystal lattices in view of the local built-in electric field around oxygen vacancy; (b) perfect crystal structure of MoO<sub>2</sub>; (c) crystal structure of MoO<sub>2</sub> with oxygen vacancy; (d) DOS of MoO<sub>2</sub> and MoO<sub>2</sub> with oxygen vacancy; (e) differential charge density distribution of oxygen vacancy in MoO<sub>2</sub>.

To explore the structure stability of the obtained electrodes, the SEM images of CN-MoO<sub>2</sub>-600 electrodes after 2 and 130 cycles at 0.1 A g<sup>-1</sup> are displayed in **Figure**

7a and b, respectively. The original morphologies of the 3D porous structure were almost inherited without obvious structural damage and agglomeration even after 130 cycles, illustrating the superior structure stability of the CN-MoO<sub>2</sub>-600 electrodes.

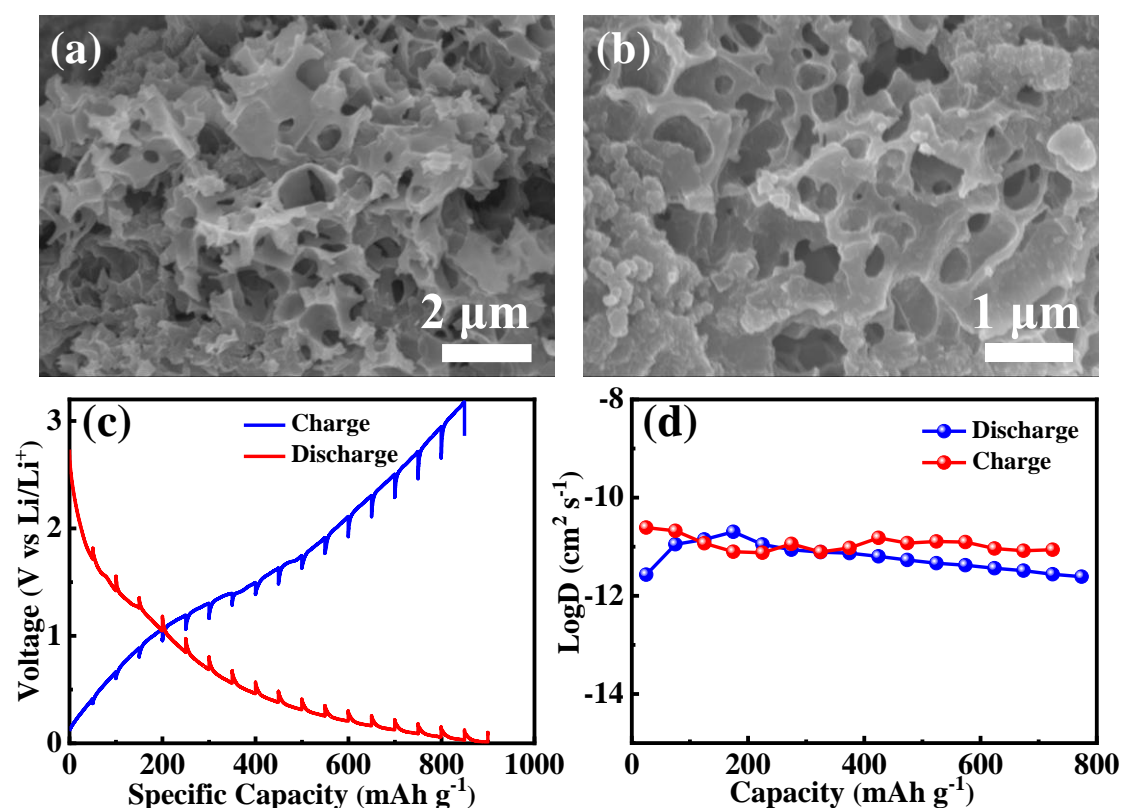
To further probe the reaction kinetics of the CN-MoO<sub>2</sub>-600 electrodes, the GITT curve and the calculated ion diffusion coefficient curve are shown in Figure 7c and d, respectively. The Li<sup>+</sup> diffusion coefficient was calculated via the galvanostatic intermittent titration technique (GITT) based on eqn (7) :

$$D = \frac{4}{\pi\tau} \left( \frac{n_m V_m}{S} \right)^2 \left( \frac{\Delta E_s}{\Delta E_t} \right)^2 \quad (7)$$

where D (cm<sup>2</sup> s<sup>-1</sup>) represents the ion diffusion coefficient,  $\tau$  (s) means the relaxation time,  $n_m$  (mol) presents the number of moles,  $V_m$  (cm<sup>3</sup> mol<sup>-1</sup>) means the molar volume of the anode material,  $S$  (cm<sup>2</sup>) means the area of the electrode piece,  $\Delta E_s$  is the voltage change induced by the pulse, and  $\Delta E_t$  is the constant current charge and discharge voltage changes. The value of D was calculated to between 10<sup>-12</sup> and 10<sup>-10</sup> cm<sup>2</sup> s<sup>-1</sup> in Figure 7d, illustrating the excellent reaction kinetic properties of CN-MoO<sub>2</sub>-600 electrodes.

**Table 1.** Comparison of the cycling performance of MoO<sub>2</sub>-based anode materials.

TMOs	Current Density A g <sup>-1</sup>	Cycle number	Capacity mAh g <sup>-1</sup>	Ref.
MoO <sub>2</sub> @RGO	1.0	50	523	[54]
MoO <sub>2</sub> @MoSe <sub>2</sub> @NC	0.5	80	468	[55]
MoO <sub>2</sub> @CNF	0.2	100	755.7	[36]
MoO <sub>2</sub> /C	1.0	1000	167	[56]
MoO <sub>2</sub> /C	1.0	400	572	[57]
MoO <sub>2</sub> /Mo <sub>2</sub> C/RGO	0.5	150	500	[58]
MoO <sub>2</sub> /Mo <sub>2</sub> C/C	0.1	100	665	[59]
3D MoO <sub>2</sub> /NC	0.1	250	912	[26]
C/MoO <sub>2</sub>	0.1	100	811	[60]
MoO <sub>2</sub> @MPCNF	1.0	500	395	[61]
MoO <sub>2</sub> /N-C	0.1	100	708	[62]
MoO <sub>2</sub> /C	1.0	1000	480	[16]
MoO <sub>2</sub> /C-G(M)	0.1	10	660	[63]
This work	<b>0.1</b>	<b>130</b>	<b>918.19</b>	
	<b>1.0</b>	<b>1000</b>	<b>562.5</b>	

**Figure 7** (a-b) SEM images of the CN-MoO<sub>2</sub>-600 electrode after 2 and 130 cycles, respectively; (c) GITT curves of CN-MoO<sub>2</sub>-600; (d) ion diffusion coefficient curve of CN-MoO<sub>2</sub>-600 electrodes.

### **3. Conclusion**

In summary, the 3D porous N-doped carbon matrix adorned with MoO<sub>2</sub> nanoparticles with oxygen vacancies was prepared via a facile and efficient route. The synthesized CN-MoO<sub>2</sub>-600 electrodes displayed outstanding electrochemical performance, including high specific capacity, satisfactory cycle stability and good rate capability, thanks to the distinctive designed morphologies, the introductions of nitrogen element and oxygen vacancies. Particularly, the oxygen vacancies act as a significant part in enhancing the electrochemical behaviors of electrodes by establishing the built-in local electric fields due to charge imbalance effects, promoting the intercalation/deintercalation of Li<sup>+</sup> by improving the reaction kinetics, which was identified by DFT and DOC calculations. The synergistic strategy of designing 3D porous structure and introducing nitrogen element and oxygen vacancies in matrix sheds light on regulating and optimizing MoO<sub>2</sub>-based and TMOs electrodes for energy storage devices.

#### **Declaration of no interest**

The authors declare that they have no known competing financial interests or personal relationships that could have appeared to influence the work reported in this paper.

#### **Acknowledgments**

This work was supported by National Natural Science Foundation of China (52207249), the research program of Top Talent Project of Yantai University (1115/2220001), Yantai Basic Research Project (2022JCYJ04) and the Science Fund

of Shandong Laboratory of Advanced Materials and Green Manufacturing (AMGM2021F11).

## References

- [1] D. Wu, X. Xie, Y. Ma, J. Zhang, C. Hou, X. Sun, X. Yang, Y. Zhang, H. Kimura, W. Du, *Chem. Eng. J.* 433 (2022) 133673.
- [2] C. Dang, Q. Mu, X. Xie, X. Sun, X. Yang, Y. Zhang, S. Maganti, M. Huang, Q. Jiang, I. Seok, W. Du, C. Hou, *Adv. Compos. Hybrid Mater.* 5 (2022) 606-626.
- [3] W. Du, X. Wang, J. Zhan, X. Sun, L. Kang, F. Jiang, X. Zhang, Q. Shao, M. Dong, H. Liu, V. Murugadoss, Z. Guo, *Electrochim Acta.* 296 (2019) 907-915.
- [4] Y. Ma, X. Xie, W. Yang, Z. Yu, X. Sun, Y. Zhang, X. Yang, H. Kimura, C. Hou, Z. Guo, W. Du, *Adv. Compos. Hybrid Mater.* 4 (2021) 906-924.
- [5] Y. Hou, C. Hou, Y. Zhai, H. Li, T. Chen, Y. Fan, H. Wang, W. Wang, *Electrochim. Acta* 324 (2019) 134884.
- [6] N. Wu, B. Zhao, X. Chen, C. Hou, M. Huang, A. Alhadhrami, G.A. Mersal, M.M. Ibrahim, J. Tian, *Adv. Compos. Hybrid Mater.* 5 (2022) 1548-1556.
- [7] W. Yang, D. Peng, H. Kimura, X. Zhang, X. Sun, R. A. Pashameah, E. Alzahrani, B. Wang, Z. Guo, W. Du, C. Hou. *Adv. Compos. Hybrid Mater.* (2022) DOI: 10.1007/s42114-022-00556-6.
- [8] X. Li, X. Sun, X. Hu, F. Fan, S. Cai, C. Zheng, G.D. Stucky, *Nano Energy* 77 (2020) 105143.
- [9] C. Hou, Y. Oaki, E. Hosono, H. Lin, H. Imai, Y. Fan, F. Dang, *Mater. Des.* 109 (2016) 718-725.
- [10] C. Hou, B. Wang, V. Murugadoss, S. Vupputuri, Y. Chao, Z. Guo, C. Wang, W. Du, *Eng. Sci.* 11 (2020) 19-30. DOI:10.30919/es8d1128
- [11] Y. Zhang, L. Liu, L. Zhao, C. Hou, M. Huang, H. Algadi, D. Li, Q. Xia, J. Wang, Z. Zhou, X. Han, Y. Long, Y. Li, Z. Zhang, Y. Liu, *Adv. Compos. Hybrid Mater.* 5 (2022) 2601-2610.
- [12] C. Hou, Z. Tai, L. Zhao, Y. Zhai, Y. Hou, Y. Fan, F. Dang, J. Wang, H. Liu, *J. Mater. Chem. A* 6 (2018) 9723-9736.
- [13] J. Zhang, A. Yu, *Sci. Bull.* 60 (2015) 823-838.
- [14] P. Zhang, S. Guo, J. Liu, C. Zhou, S. Li, Y. Yang, J. Wu, D. Yu, L. Chen, *J. Colloid Interface Sci.* 563 (2020) 318-327.

- [15] C. Zheng, W. Wu, Q. Deng, Y. Li, M. Wei, J. Colloid Interface Sci. 592 (2021) 33-41.
- [16] Y. Yao, Z. Chen, R. Yu, Q. Chen, J. Zhu, X. Hong, L. Zhou, J. Wu, L. Mai, ACS Appl. Mater. Interfaces 12 (2020) 40648-40654.
- [17] G. Liu, F. Xiao, T. Zhang, Y. Gu, J. Li, D. Guo, M. Xu, N. Wu, A. Cao, X. Liu, Appl. Surf. Sci. 597 (2022) 153688.
- [18] S. Petnikota, K.W. Teo, L. Chen, A. Sim, S.K. Marka, M.V. Reddy, V.V. Srikanth, S. Adams, B.V. Chowdari, ACS Appl. Mater. Interfaces 8 (2016) 10884-10896.
- [19] Y. Zhang, K. Ruan, J. Gu, Small 17 (2021) 2101951.
- [20] K. Ruan, Y. Guo, J. Gu, Macromol. 54 (2021), 4934-4944.
- [21] Z. Ma, X. Xiang, L. Shao, Y. Zhang, J. Gu, Angew. Chem. Int. Ed. 61 (2022) e202200705.
- [22] Y. Zhang, J. Kong, J. Gu, Sci. Bull. 67 (2022) 1413-1415.
- [23] K. Ruan, J. Gu, Macromol. 55 (2022), 4134-4145.
- [24] X. Liu, M. Gao, J. Chen, S. Guo, W. Zhu, L. Bai, W. Zhai, H. Du, H. Wu, C. Yan, Y. Shi, J. Gu, H. Qi, K. Zhou, Adv. Funct. Mater. 32 (2022) 2203323.
- [25] X. Xie, Y. Wang, X. Sun, H. Wang, R. Yu, W. Du, H. Wu, J. Mater. Sci. Technol. 133 (2023) 1-11.
- [26] H. Wang, X. Jiang, Y. Wang, X. Yang, Y. Chai, Z. Yu, M. Xu, R. Yuan, Powder Technol. 377 (2021) 281-288.
- [27] Y. Zhai, W. Yang, X. Xie, X. Sun, J. Wang, X. Yang, N. Naik, H. Kimura, W. Du, Z. Guo, C. Hou, Inorg. Chem. Front. 9 (2022) 1115-1124.
- [28] Z.K. Tang, Y.F. Xue, G. Teobaldi, L.M. Liu, Nanoscale Horiz. 5 (2020) 1453-1466.
- [29] D. Luo, G. Li, Y.P. Deng, Z. Zhang, J. Li, R. Liang, M. Li, Y. Jiang, W. Zhang, Y. Liu, W. Lei, A. Yu, Z. Chen, Adv. Energy Mater. 9 (2019) 1900228.
- [30] C. Hou, G. Fan, X. Xie, X. Zhang, X. Sun, Y. Zhang, B. Wang, W. Du, R. Fan, J. Alloys Compd. 855 (2021) 157499.
- [31] Q. Li, Y. Zhao, H. Liu, P. Xu, L. Yang, K. Pei, Q. Zeng, Y. Feng, P. Wang, R. Che, ACS Nano 13 (2019) 11921-11934.
- [32] C. Hou, Y. Hou, Y. Fan, Y. Zhai, Y. Wang, Z. Sun, R. Fan, F. Dang, J. Wang, J. Mater. Chem. A 6 (2018) 6967-6976.

- [33] X. Liu, P. Mei, Y. Dou, R. Luo, Y. Yamauchi, Y. Yang, *J. Mater. Chem. A* 9 (2021) 13001-13007.
- [34] Z.K. Kong, Y. Chen, J.Z. Hua, Y.Z. Zhang, L. Zhan, Y.L. Wang, *New Carbon Mater.* 36 (2021) 810-820.
- [35] Q. Hao, G. Cui, Y. Zhang, J. Li, Z. Zhang, *Chem. Eng. J.* 381 (2020), 122672.
- [36] H. Zhang, Z. Han, X. Li, F. Kong, S. Tao, B. Qian, *Ceram. Int.* 47 (2021) 26839-26846.
- [37] M. Yang, Q. Kong, W. Feng, W. Yao, Q. Wang, *Appl. Surf. Sci.* 569 (2021) 150984.
- [38] Y. Feng, H. Liu, *Appl. Surf. Sci.* 538 (2021) 147992.
- [39] C. Liu, P.K. Fan, X.Q. Xie, Y.J. Sun, Y. Li, X.J. Wang, *J. Colloid Interface Sci.* 623 (2022) 267-276.
- [40] S. Zhu, J. Fan, Y. Yang, L. You, X. Wu, *J. Electroanal. Chem.* 917 (2022) 116414.
- [41] J. Tang, J. Xu, L. Li, Y. Ma, Z. Ye, H. Luo, J. Luo, *Trans. Nonferrous Met. Soc. China* 32 (2022) 1598-1608.
- [42] S. Yuan, M. Xia, Z. Liu, K. Wang, L. Xiang, G. Huang, J. Zhang, N. Li, *Chem. Eng. J.* 430 (2022) 132697.
- [43] Y. Zhang, H. Wu, Z. Liu, S. Xie, J. Li, *J. Materiomics* 7 (2021) 347-354.
- [44] W. Tian, H. Hu, Y. Wang, P. Li, J. Liu, J. Liu, X. Wang, X. Xu, Z. Li, Q. Zhao, H. Ning, W. Wu, M. Wu, *ACS Nano* 12 (2018) 1990-2000.
- [45] Y. Chen, H. Chen, F.H. Du, X. Shen, Z. Ji, H. Zhou, A. Yuan, *J. Alloys Compd.* 926 (2022) 166847.
- [46] J. Ding, Y. Huang, Z. Liu, X. Wang, Y. Zhang, Y. Guo, R. Sheng, D. Jia, X. Tang, L. Wang, *Chem. Eng. J.* 431 (2022) 133984.
- [47] J. Li, H. Wei, F. Hu, Z. Xie, J. Hei, Y. Kong, X. Yin, N. Wang, H. Wei, *Int. J. Hydrogen Energy.* 47 (2022) 32594-32606.
- [48] W. Yang, L. Han, X. Liu, L. Hong, M. Wei, *J. Colloid Interface Sci.* 588 (2021) 804-812.
- [49] H. Sun, J. Xu, J. Huang, G. Li, J. Luo, M. Rao, Z. Peng, T. Jiang, *J. Alloys Compd.* 851 (2021), 156726.
- [50] C. Hou, W. Yang, X. Xie, X. Sun, J. Wang, N. Naik, D. Pan, X. Mai, Z. Guo, F. Dang, W. Du, *J. Colloid Interface Sci.* 596 (2021) 396-407.

- [51] H. Wang, H. Wang, D. Zhang, G. Chen, L. Chen, N. Zhang, R. Ma, X. Liu, ACS Appl. Mater. Interfaces 13 (2021) 19836-19845.
- [52] C. Hou, J. Wang, W. Du, J. Wang, Y. Du, C. Liu, J. Zhang, H. Hou, F. Dang, L. Zhao, Z. Guo, J. Mater. Chem. A 7 (2019) 13460-13472.
- [53] C. Hou, J. Wang, W. Zhang, J. Li, R. Zhang, J. Zhou, Y. Fan, D. Li, F. Dang, J. Liu, Y. Li, K. Liang, B. Kong, ACS Appl. Mater. Interfaces 12 (2020) 13770-13780.
- [54] X. Chen, R. Liu, L. Zeng, X. Huang, Y. Fang, J. Liu, Y. Xu, Q. Chen, M. Wei, Q. Qian, Mater. Lett. 212 (2018) 198-201.
- [55] Z. Qin, X. Liu, Z. Huang, R. Sun, Z. Li, H. Fan, S. Lu, Acta Metall. Sin. Engl. 34 (2021) 425-434.
- [56] J. Huo, Y. Xue, Y. Liu, Y. Ren, G. Yue, J. Electroanal. Chem. 857 (2020) 113751.
- [57] C. Lingfei, Y. Liu, G. Zhang, R. Zhang, Microporous Mesoporous Mater. 327 (2021) 111427.
- [58] W. Devina, J. Hwang, J. Kim, Chem. Eng. J. 345 (2018) 1-12.
- [59] X. Li, Q. Xiao, H. Zhang, H. Xu, Y. Zhang, J. Energy Chem. 27 (2018) 940-948.
- [60] J. Xiang, Z. Wu, X. Zhang, S. Yao, Mater. Res. Bull. 100 (2018) 254-258.
- [61] X.H. Zhou, Y. Gao, L.H. Lyu, Y.Y. Liang, Z.H. Li, Carbon 179 (2021) 142-150.
- [62] H. Sun, Y. Zhang, H. Liu, X. Zhang, J.G. Wang, J. Alloys Compd. 787 (2019) 45-52.
- [63] G.S. Zakharova, L. Singer, Z.A. Fattakhova, S. Wegener, E. Thauer, Q. Zhu, E.V. Shalaeva, R. Klingeler, J. Alloys Compd. 863 (2021) 158353.